Visible light $Bi_2S_3/BiFeO_3$ photocatalyst for effective removal of Rhodamine B

Xiquan Wang[1], Nan Zhang[1,a] and Gao Wang[1]

[1] *School of Chemical Engineering, University of Science and Technology Liaoning, High-Tech District,185 Qian shan Middle Road, Anshan 114051, China.*

Abstract: Bi_2S_3-sensitized $BiFO_3$ (BFO) photocatalyst (Bi_2S_3/BFO) was successfully synthesized through a facile and environmental ion exchange method between BFO and Thiourea (H_2NCSNH_2, TU). The photocatalysts were characterized by X-ray diffraction (XRD), scanning electron microscopy (SEM), energy-dispersive X-ray spectroscopy (EDS) and UV-vis diffuse reflection spectroscopy (DRS). The obtained Bi_2S_3/BFO composites showed excellent photocatalytic performance for decomposing Rhodamine B (RhB) compared with pure BFO under visible light irradiation (λ>400nm). 5% Bi_2S_3/BFO exhibited the highest photocatalytic activity and excessive amount of Bi_2S_3 would result in the decrease of photocatalytic activity of BFO. The mechanism of enhanced photocatalytic activity was proposed on the basis of the calculated energy band positions.

1 Introduction

Photocatalysis has received much attention owing to current environment concerns and energy demand[1]. Visible-light-responding photocatalysts have attracted increasing interest in the past years due to their potential applications in splitting of water and degradation of organic pollutants under visible light irradiation. Recently, a growing number of investigations on exploitation of Bi-containing compounds, such as $BiVO_4$[2, 3], Bi_2MoO_6 [4], Bi_2WO_6[5, 6], have been undertaken. A series of researches have revealed that whether Bi^{3+}-containing or Bi^{5+}-containing compounds have exhibited high photocatalytic ability in visible light range, which is ascribed to the hybridized valence band (VB) of O 2p and Bi 6s that narrows the band gap[7]. As a member of Bi-based multi-component oxides, typical Rhombohedral structure BFO has been widely studied because of its special properties, such as narrow band gap (2.0-2.7eV), ferroelectric and ferromagnetic properties[8]. BFO had been considered as one of the third-generation visible-light responsive photocatalyst. Gao et al.[9] synthesized perovskite-type BFO photocatalysts via a facile hydrothermal method and used it to degradat Methyl Orange under visible-light irradiation. Gao et al.[10] also synthesized perovskite phase material BFO by simple sol-gel route and evaluated the photocatalytic performance on visible-light degradation of Methyl Orange. However, research concerning the improvement of visible light photocatalytic properties of BFO is still scarce.

Up to now, previous studies had showed that semiconductor combine with other semiconductors could extend the spectral responsive range, separate the charge carriers effectively and further enhance photocatalytic activity of single-component materials dramatically[11, 12]. Especially the construction of Bi_2S_3 heterostructured composites has considered as an attractive and promising method. Bismuth sulfide (Bi_2S_3) is a typical layered band-gap semiconductor with a narrow band gap (1.3-1.7eV) and large absorption coefficient[13], which has been used for electrochemical hydrogen storage[14], hydrogen sensor[15], biomolecule detection[16], X-ray computed tomography imaging[17], and photo-responsive materials[18]. Because of its narrow band-gap, it was used as a potential visible light photocatalyst through combine with Bi_2O_3[19, 20], $BiVO_4$[21], $Bi_2Sn_2O_7$[22], $Bi_4Ti_3O_{12}$[23] and BiOCl[24, 25]. However, Bi_2S_3/BFO composite photocatalysts have never been reported.

Herein, we mention a new combination route preparation of sol-gel and solvothermal process for Bi_2S_3/BFO composites. Rhodamine B (RhB) as a model pollutant under visible light (lambda >400nm) evaluated the photocatalytic performance, results showed that the photocatalytic activity of Bi_2S_3/BFO composite is better than pure BFO. In addition, also studied the mechanism of Bi_2S_3/BFO composites.

[a] Corresponding author: Tel: 86 18341277889;Email:2387923823@qq.com

2 Experimental

2.1 Chemical and materials

All the chemical materials without further processing used during experiment were analytically pure . Iron nitrate ($Fe(NO_3)_3·9H_2O$), Bismuth Nitrate ($Bi(NO_3)_3·5H_2O$), Thiourea (CN_2H_4S, TU), Ethylene Glycol ($C_2H_6O_2$), Hydrochloric Acid(HCl) and absolute Ethyl Alcohol (C_2H_6O) were obtained from Quan Rui Chemical Reagent Co., Ltd (Liao Ning, China). Rhodamine B ($C_{28}H_{31}ClN_2O_3$, RhB) was provided by Dong Xing chemical (Liao Ning, China). The wastewater was simulated by dissolving 10 mg/L RhB to the deionized water.

2.2. Preparation of BFO nanoparticles

The BFO nanoparticles sample was prepared through a sol-gel method according to previous studies[10]. In a typical synthesis, BFO powders were synthesized by a simple sol-gel route. $Bi(NO_3)_3·5H_2O$ and $Fe(NO_3)_3·9H_2O$ of 0.02 mol (1:1 molar ratio) were dissolved in 50 mL Ethylene Glycol as precursor solution, and the final concentration was 0.4 mol/L. The mixture was stirred for about 1.5 h at 80°C to obtain the sol. The gel was kept at 120°C for 4 days to form a xerogel powder. Then the powder was heated at 300°C for 3 h as a pretreatment. The final powder was calcined at the temperatures of 500°C for 2 h under air condition.

2.3. Synthesis of Bi_2S_3/BFO composites

In order to synthesize Bi_2S_3/BFO composites, 0.1564 g of as-prepared BFO was dispersed in 20mL absolute Ethyl Alcohol under ultrasonic.A certain amount of TU dissolved in absolute Ethyl Alcohol was added dropwise to the BFO solution.Finally, transferred the appropriate absolute Ethyl Alcohol to the mixture to make the volume reach 24mL.After sonication for 30 min, put 30mL of solution into a Teflon-lined stainless steel autoclave and heated at 180°C for 6 h. Finally, the precipitates of Bi_2S_3/BFO with different theoretical molar percentage of Bi_2S_3 and initial BFO (from 2.5 to 50%) were collected, washed and dried at 80°C.

For comparison, the bulk Bi_2S_3 sample was prepared through a hydrothermal process according to Ref[26]. $Bi(NO_3)_3·5H_2O$ and TU were mixed in deionized water (1:2.5 molar ratio) at 140°C for 12 h.

2.4 Characterization of catalyst

The phases of the samples were examined by X-ray diffraction (XRD) on a Philips X'pert PRO diffractometer with Cu K_α radiation. The size and morphology of the prepared samples were observed by scanning electronmicroscope (SEM, Carl Zeiss EVO LS-15). Chemical analysis of the photocatalyst was performed by X-ray analysis (EDS) in a CarlZeiss EVO LS-15 scanning electronmicroscopy (SEM). The UV–Vis diffuse reflectance spectrum (UV-DRS) of the powders were measured by a UV–Vis spectrophometer (Gucun ZF-I) equipped.

2.5. Degradation experiment

The photocatalytic performance of the photocatalysts were evaluated by the degradation of RhB under visible light irradiation. The visible light source was a 150 W halogen tungsten lamp (λ_{max}= 588 nm) with the combination of a cut-off filter (λ> 400 nm) to eliminate UV radiation during visible light experiments. The system was cooled by wind and water and maintained at room temperature. In every run, 100mg Bi_2S_3/BFO was added to 100mL RhB solution (10mg/L) in a Pyrex vessel. Before the experiment, the suspension was magnetically stirred in the dark for 1 h to ensure the establishment of an adsorption–desorption equilibrium of the dye on the catalysts' surfaces. Under visible light irradiation, samples were regularly extracted and the catalyst powders were centrifugally removed. The residual RhB concentration was monitored by measuring the absorbance of the solution at the characteristic absorption wavelength of 554nm for RhB with a UV-Vis spectrophotometer (UV-5100, Metash) at room temperature. The photocatalytic efficiency was calculated by the decolouration percentage: $\eta = C/C_0 \times 100\%$, where the C is the final dye concentration, C0 is the initial concentration of dye.

3 Result and discussion

3.1. Crystalline property

In this study, BFO nano-materials was prepared by a sol-gel process with $Bi(NO_3)_3·5H_2O$ and $Fe(NO_3)_3·9H_2O$ in ethylene glycol solvent followed by heating, calcining and collecting in the first place. Then, the process of product synthesis is as follows.

$$4Fe(NO_3)_3 \rightarrow 2Fe_2O_3 + 12NO_2 + 3O_2 \quad (1)$$

$$4Bi(NO_3)_3 \rightarrow 2Bi_2O_3 + 12NO_2 + 3O_2 \quad (2)$$

$$Fe_2O_3 + Bi_2O_3 \rightarrow 2BiFeO_3 \quad (3)$$

The composition and phase structures of the as-prepared samples were examined by XRD. Fig. 1 presents the XRD patterns of pure BFO, Bi_2S_3 and Bi_2S_3/BFO with different Bi_2S_3 contents. It can be observed that all the samples are well crystallized. The diffraction peaks of pure BFO could be indexed to the standard PDF card of rhombohedral BFO (JCPDS No.86-1518) , as well as the feature peaks of the pure Bi_2S_3 are clearly corresponding to the orthorhombic structure of Bi_2S_3 (JCPDS No.17-0320). No impurity peaks were detected, implying that the final products of Bi_2S_3 and BFO are pure phases.

Furthermore, when the amount of Bi_2S_3 is below 10%, there are no diffraction peaks of Bi_2S_3 that can be observed, which may be due to the low content of Bi_2S_3 below the XRD detection limit. However, when the amount of Bi_2S_3 reaches 25%, the peaks of (130) and (211) planes of orthorhombic Bi_2S_3 appear. Moreover, when the amount of Bi_2S_3 reaches 50%, the peak of (240) planes of orthorhombic Bi_2S_3 is appearance. In addition, with the molar percentage of Bi_2S_3 increasing, the intensities of diffraction peaks of Bi_2S_3 increase whereas those of BFO

decrease. Therefore, the above results suggest that Bi_2S_3/BFO composites can be successfully synthesized by a solvothermal method.

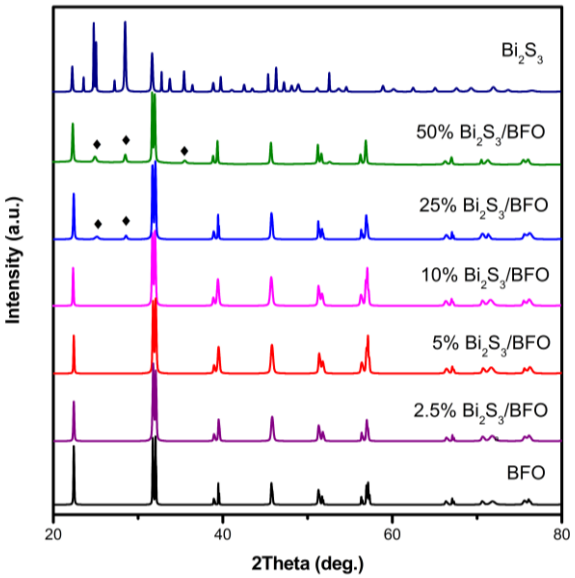

Figure 1. XRD patterns of BFO, Bi_2S_3 and Bi_2S_3/BFO composites with different Bi_2S_3 contents.

3.2. Morphology analysis

Fig. 2 shows SEM images of BFO and B_2S_3/BFO composites with different Bi_2S_3 contents. For comparison, the morphology of BFO nanoparticles which is annealed at 500°C with the concentration of 0.4 mol/L precursor solution was shown in fig. (a), revealing that the size of BFO materials pose irregular morphology with mean sizes below 100 nm. The Bi_2S_3/BFO samples exhibit two structures: a nanorod shape and a irregular shape particles, as shown in Fig. 2(b), (c), and (e-h). According to previous studies and these images, we can deduce that nanorod shape particles and polygonal shape particles are Bi_2S_3 and BFO respectively. At the same time, EDS analysis of the nanorods (Fig. 2d) suggests that the nanorods are composed of Bi and S elements, further confirming the result of XRD. All these above confirm the formation of Bi_2S_3 on BFO.

3.3 UV-vis DRS analysis

Fig. 3 displays the UV-vis diffuse reflection spectrum (DRS) of the as-prepared samples. It can be observed that all the samples displayed absorption in the visible light region and pure Bi_2S_3 appeared strong absorption over the whole visible light region. For Bi_2S_3/BFO composites, the absorption band is similar to the pure BFO, and the edge of absorption band moves towards long wavelength gradually. The absorption intensity increases with the increase of Bi_2S_3 content in 500-800 nm region, which is due to the high visible light response of Bi_2S_3.

For a semiconductor, theoretically, the optical absorption near the band edge follows the formula: $\alpha h\nu = A(h\nu - E_g)^{n/2}$[27], where α, ν, E_g, and A are the absorption coefficient, light frequency, band-gap energy, and a constant, respectively. The value of n depends on

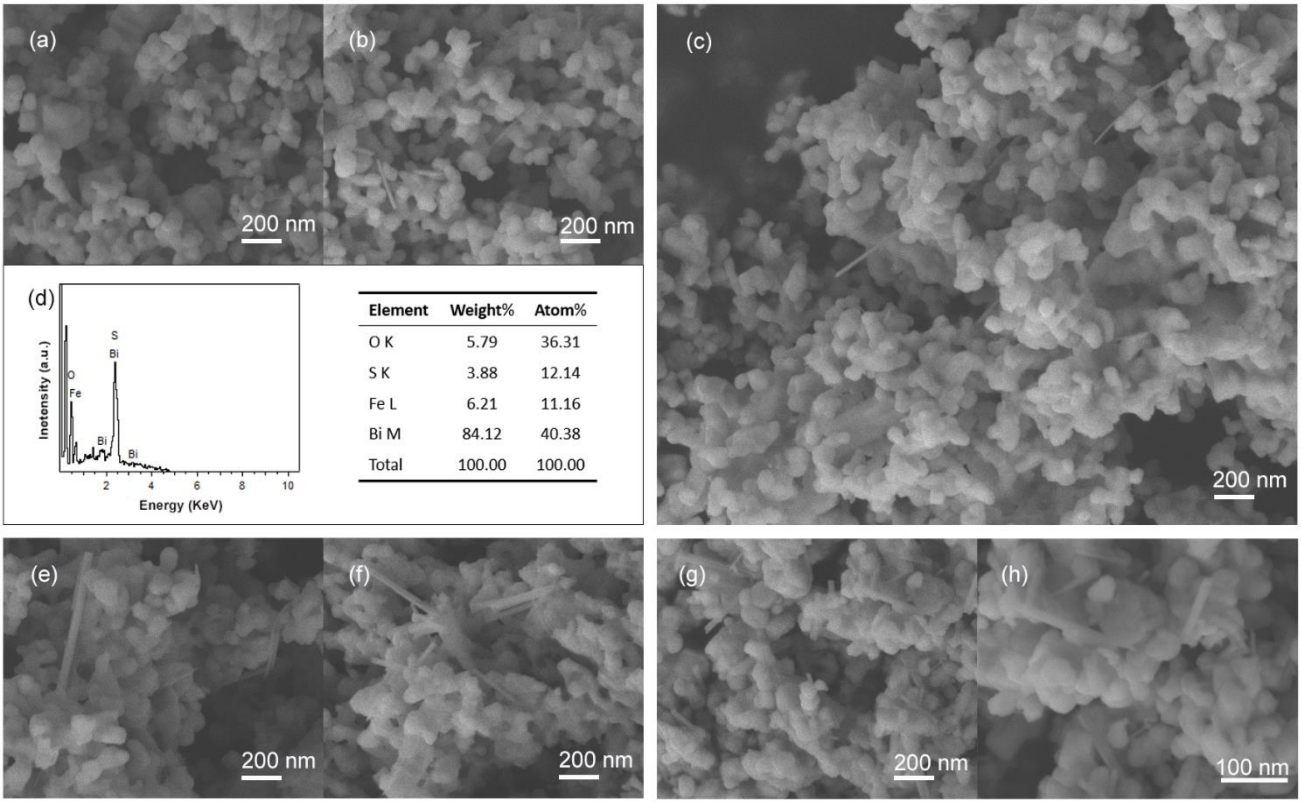

Figure 2. SEM images of (a) BFO and also B_2S_3/BFO composites with different Bi_2S_3contents: (b) 2.5%, (c) 5%, (e) 10%, (f) 25%, and (g & h) 50%. Also EDS spectrum of the Bi_2S_3/BFO composites.

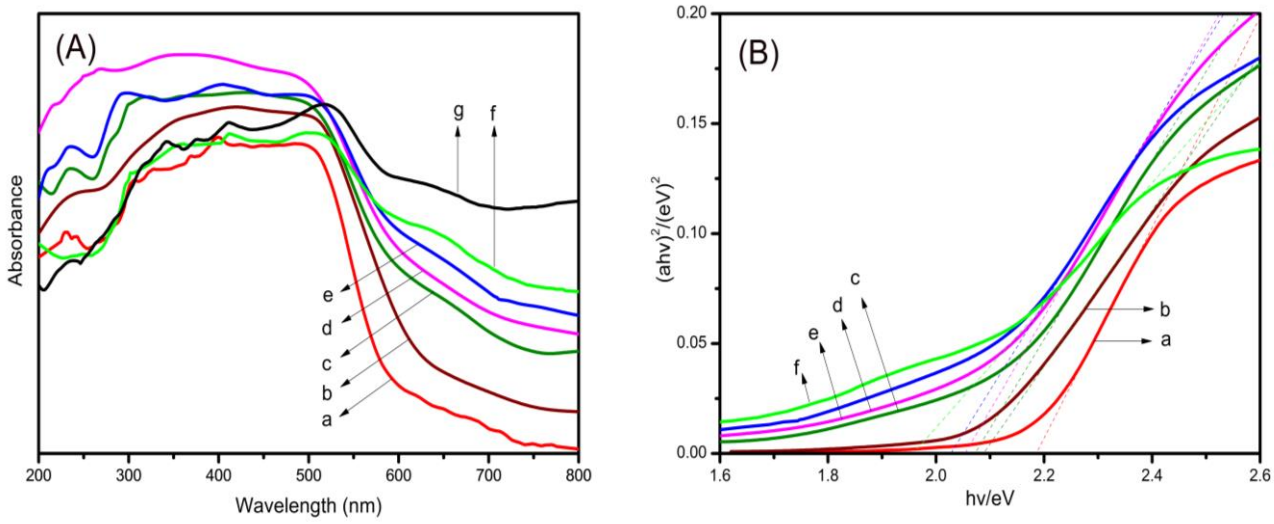

Figure 3. (A) UV–vis diffuse reflectances spectra and (B) Plot of $(\alpha hv)^2$ vs. energy (hv) for the band-gap energy of (a) BFO, (g) Bi_2S_3 and Bi_2S_3/BFO samples with different Bi_2S_3 contents: (b) 2.5 %, (c) 5 %, (d) 10 %, (e) 25 %, (f) 50 %.

whether the transition is direct (n = 1) or indirect (n = 4) in a semiconductor. For BFO and Bi_2S_3, they pertain to direct transition. Thus, n is equal to 1. Fig. 6b shows the curve of $(\alpha hv)^2$ versus hv. On the basis of the extrapolation, the band gap energy (E_g) of BFO and 2.5, 5, 10, 25, 50% Bi_2S_3/ BFO are respectively estimated to be about 2.18, 2.09, 2.07, 2.06, 2.03 and 1.96 eV, which is attributed to the quantum confinement of Bi_2S_3 nanocrystals. Otherwise, the well-crystallized Bi_2S_3 samples have a band gap close to 1.3 eV, and exhibit considerable absorption strength in almost all visible light ranges.

3.4 Photocatalytic activity test

The photocatalytic activities of the prepared products were evaluated by photodegradation of RhB under visible light irradiation (λ>400nm). Fig. 4a shows the change of absorption spectra of RhB aqueous when the Bi_2S_3/BFO content is 5% after 3 h. It can be seen from the spectra that the major absorption peaks of RhB at 554 nm gradually decreased as the irradiation time increases and blue shifted step by step. The results show that the ethyl groups are removed one by one which is consistent with the literature description. And compared with pure BFO and Bi_2S_3, 5% Bi_2S_3/BFO shows the excellent photocatalytic activity for the RhB degradation. Furthermore, the stepwise blue shift of the main peak can be attributed to the formation of the de-methylated of RhB[28].

Fig. 4b shows the photocatalytic activities of different catalysts. For comparison, carried out the same degradation experiment in the absence of photocatalyst which shows no
appreciable degradation of RhB after irradiating for 3 h. Also, in the presence of pure BFO and Bi_2S_3 only about 62.6% and 11.1% of RhB concentration were decomposed after irradiation for 3 h, which could attributed to the high stability and negligible self-photolysis of RhB. The dark adsorption abilities for RhB were 14.4%, 12.1%, 32.5% and 19.6% for 2.5%, 5%, 10%, 25% Bi_2S_3/BFO samples, respectively. The activities of the four types of Bi_2S_3/BFO photocatalysts were better than that of BFO, arising from their visible light responsive behaviors. The highest

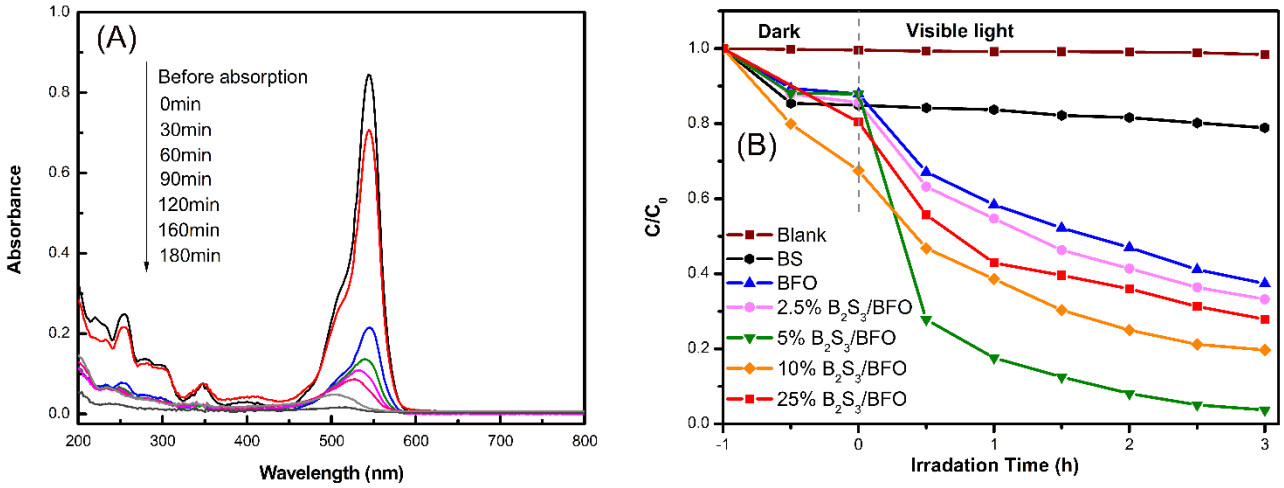

Figure 4. (A) UV-Vis spectral changes during the photodegradation of RhB mediated by 5% Bi_2S_3/BFO sample and (B) Photocatalytic activities of different catalysts.

activity was obtained over the 5% Bi_2S_3/BFO sample, on which more than 96.3% of RhB was degraded within 3 h. Clearly, the content of Bi_2S_3 dramatically affect the photocatalytic activities of Bi_2S_3/BFO catalysists even though the content was very low. RhB was decomposed into 66.8%, 80.3% and 72.1% after 3 h irradiation with 2.5% Bi_2S_3/BFO, 10% Bi_2S_3/BFO and 25% Bi_2S_3/BFO respectively. Therefore, it can be observed that the photocatalytic activities of the Bi_2S_3/BFO composites increase and then decline with the increase of irradiate time. According to the Langmuir-Hinshelwood reaction kinetics model, the photocatalytic oxidation of Bi_2S_3/BFO is a first-order reaction.

3.5 The energy band structure and possible photocatalytic mechanism

Whether Bi_2S_3/BFO heterostructure is conducive to the separation of photo-generated carriers or not is closely related to their band-edge positions. The valence band (VB) edge and the conduction band (CB) edge positions of Bi_2S_3/BFO were calculated empirically according to formula[27]:

$$E_{VB}=\chi-E^e+0.5E_g \quad (4)$$

$$E_{CB}=E_{VB}-E_g \quad (5)$$

where EVB is the valence band-edge potential, χ is the electronegativity of the semiconductor, which is defined as the geometric mean of the absolute electronegativity of the constituent atoms, Ee is the energy of free electrons on the hydrogen scale (ca. 4.5 eV), Eg is the band gap energy of the semiconductor. The χ values of BFO and Bi_2S_3 were 5.74 eV and 5.28 eV[22, 29], respectively. The band-gap energies of BFO and Bi_2S_3 are 2.18 eV and 1.3 eV. Given the equation above, the top of the valence band (VB) and the bottom of the conduction band (CB) of BFO and Bi_2S_3 are calculated to be 2.33, 0.14 and 1.48, 0.09 eV. Both the CB and the VB of Bi_2S_3 are higher than those of pure BFO. Obviously, the difference between energy bands of BFO and Bi_2S_3 demonstrated the heterostructure of Bi_2S_3/BFO is propitious to the separation and transportation of charge carriers.

Based on the above results, the energy band levels of Bi_2S_3/BFO and the possible charge-separation process are shown in Fig. 5 Under visible-light irradiation, Bi_2S_3 and BFO are both easily excited and photo-induced electrons and holes are generated correspondingly. Due to the higher CB position of Bi_2S_3 than that of BFO photo-generated electrons in Bi_2S_3 could transfer to the CB of BFO and the photo-generated holes in the VB of BFO migrate to Bi_2S_3 because of the less positive VB of Bi_2S_3 than that of BFO. Thus, the photo-induced electrons and holes can be efficiently separated and RhB will be oxidized to the final products. The redox potential of O_2/OH^- is 0.401 eV, the electrons located on the CB of BFO (E_{CB}=0.14 eV) can reduce O_2 to OH^-. However, the photo-generated holes at the VB of Bi_2S_3 with potential of 1.48 eV, which is more negative than the standard reduction potential of $OH^-/\cdot OH$ (1.99 eV)[22], can´t oxidize OH^- to ·OH. Therefore, this result indicated that the active species are photogenerated holes that play more important role in the photodegradation process of RhB rather than ·OH.

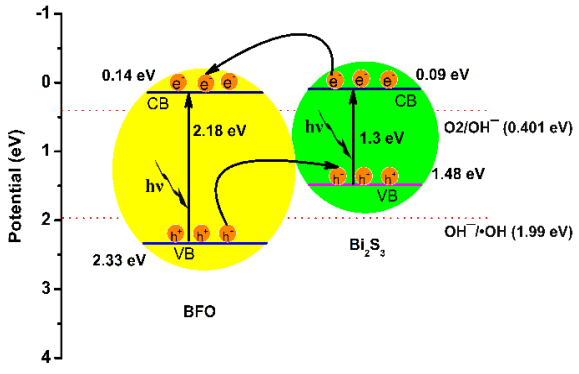

Figure 5. Diagram for energy band levels of Bi_2S_3/BFO composites and the possible charge separation process.

4 Conclusions

In summary, Bi_2S_3/BFO composites have been successfully synthesized through a facile and economical ion exchange method. The prepared Bi_2S_3/BFO photocatalyst with high photocatalytic activity of RhB under visible light irradiation, is about two times higher than the pure BFO photocatalyst. The content of Bi_2S_3 played an important role to the photocatalytic activities and the optimal content of Bi_2S_3 was 5% with maximal photocatalytic degradation efficiency of 96.3%. This result could be attributed to the good visible light absorption of Bi_2S_3 and the effective separation of electron-holes pairs due to the formation of heterojunction between the two semiconductors. The composites displayed much higher activity than the individual components towards the degradation of RhB under visible-light irradiation, suggesting that they are new types of visible-light-driven photocatalysts for water purification application and environmental remediation. Therefore, this study provides a new and simple way to prepare composite nanomaterials.

References

1. H. Tong, S. Ouyang, Y. Bi, N. Umezawa, M. Oshikiri, J. Ye, Nano-photocatalytic materials: possibilities and challenges, Advanced materials (Deerfield Beach, Fla.), **24** (2012) 229-251.
2. T.W. Kim, K.S. Choi, Nanoporous $BiVO_4$ Photoanodes with Dual-Layer Oxygen Evolution Catalysts for Solar Water Splitting, Science, **343** (2014) 990-994.
3. Y.H. Ng, A. Iwase, A. Kudo, R. Amal, Reducing Graphene Oxide on a Visible-Light $BiVO_4$ Photocatalyst for an Enhanced Photoelectrochemical Water Splitting, Journal of Physical Chemistry Letters, **1** (2010) 2607-2612.
4. G. Tian, Y. Chen, W. Zhou, K. Pan, Y. Dong, C. Tian, H. Fu, Facile solvothermal synthesis of hierarchical flower-like Bi_2MoO_6 hollow spheres as high performance visible-light driven photocatalysts, Journal of Materials Chemistry, **21** (2011) 887-892.
5. L. Ge, C.C. Han, J. Liu, Novel visible light-induced g-C_3N_4/Bi_2WO_6 composite photocatalysts for efficient

degradation of methyl orange, Applied Catalysis B-Environmental, **108** (2011) 100-107.
6. H.L. Wang, L.S. Zhang, Z.G. Chen, J.Q. Hu, S.J. Li, Z.H. Wang, J.S. Liu, X.C. Wang, Semiconductor heterojunction photocatalysts: design, construction, and photocatalytic performances, Chemical Society reviews, **43** (2014) 5234-5244.
7. R.a. He, S. Cao, P. Zhou, J. Yu, Recent advances in visible light Bi-based photocatalysts, Chinese Journal of Catalysis, **35** (2014) 989-1007.
8. Y. Li, X. Fang, M. Cao, Thermal frequency shift and tunable microwave absorption in $BiFeO_3$ family, Scientific reports, **6** (2016) 24837.
9. T. Gao, Z. Chen, F. Niu, D. Zhou, Q. Huang, Y. Zhu, L. Qin, X. Sun, Y. Huang, Shape-controlled preparation of bismuth ferrite by hydrothermal method and their visible-light degradation properties, Journal of Alloys and Compounds, **648** (2015) 564-570.
10. T. Gao, Z. Chen, Y. Zhu, F. Niu, Q. Huang, L. Qin, X. Sun, Y. Huang, Synthesis of $BiFeO_3$ nanoparticles for the visible-light induced photocatalytic property, Materials Research Bulletin, **59** (2014) 6-12.
11. C. Chen, W. Ma, J. Zhao, Semiconductor-mediated photodegradation of pollutants under visible-light irradiation, Chemical Society reviews, **39** (2010) 4206-4219.
12. X. Chen, S. Shen, L. Guo, S.S. Mao, Semiconductor-based Photocatalytic Hydrogen Generation, Chemical Reviews, **110** (2010) 6503-6570.
13. M.T.S. Nair, P.K. Nair, Photoconductive bismuth sulphide thin films by chemical deposition, Semiconductor Science and Technology, **5** (1990) 1225.
14. L. Li, N. Sun, Y. Huang, Y. Qin, N. Zhao, J. Gao, M. Li, H. Zhou, L. Qi, Topotactic Transformation of Single-Crystalline Precursor Discs into Disc-Like Bi_2S_3 Nanorod Networks, Advanced Functional Materials, **18** (2008) 1194-1201.
15. K. Yao, W.W. Gong, Y.F. Hu, X.L. Liang, Q. Chen, L.M. Peng, Individual Bi_2S_3 Nanowire-Based Room-Temperature H_2 Sensor, The Journal of Physical Chemistry C, **112** (2008) 8721-8724.
16. O. Rabin, J. Manuel Perez, J. Grimm, G. Wojtkiewicz, R. Weissleder, An X-ray computed tomography imaging agent based on long-circulating bismuth sulphide nanoparticles, Nature materials, **5** (2006) 118-122.
17. K.L. Ai, Y.L. Liu, J.H. Liu, Q.H. Yuan, Y.Y. He, L.H. Lu, Large-Scale Synthesis of Bi_2S_3 Nanodots as a Contrast Agent for In Vivo X-ray Computed Tomography Imaging, Advanced Materials, **23** (2011) 4886-4891.
18. T. Wu, X.G. Zhou, H. Zhang, X.H. Zhong, Bi_2S_3 Nanostructures: A New Photocatalyst, Nano Research, **3** (2010) 379-386.
19. Y. Yan, Z. Zhou, X. Zhao, J. Zhou, A controlled anion exchange strategy to synthesize core-shell beta-bismuth oxide/bismuth sulfide hollow heterostructures with enhanced visible-light photocatalytic activity, Journal of colloid and interface science, **435** (2014) 91-98.
20. L. Chen, J. He, Q. Yuan, Y. Liu, C.-T. Au, S.-F. Yin, Environmentally benign synthesis of branched Bi_2O_3–Bi_2S_3 photocatalysts by an etching and re-growth method, J. Mater. Chem. A, **3** (2015) 1096-1102.
21. X. Gao, H.B. Wu, L. Zheng, Y. Zhong, Y. Hu, X.W. Lou, Formation of Mesoporous Heterostructured $BiVO_4$/Bi_2S_3 Hollow Discoids with Enhanced Photoactivity, Angewandte Chemie, **126** (2014) 6027-6031.
22. W. Xu, J. Fang, Y. Chen, S. Lu, G. Zhou, X. Zhu, Z. Fang, Novel heterostructured Bi_2S_3/$Bi_2Sn_2O_7$ with highly visible light photocatalytic activity for the removal of Rhodamine B, Materials Chemistry and Physics, **154** (2015) 30-37.
23. Y. Liu, M. Zhang, L. Li, X. Zhang, In situ ion exchange synthesis of the $Bi_4Ti_3O_{12}$/Bi_2S_3 heterostructure with enhanced photocatalytic activity, Catalysis Communications, **60** (2015) 23-26.
24. S. Jiang, K. Zhou, Y. Shi, S. Lo, H. Xu, Y. Hu, Z. Gui, In situ synthesis of hierarchical flower-like Bi_2S_3/BiOCl composite with enhanced visible light photocatalytic activity, Applied Surface Science, **290** (2014) 313-319.
25. H. Cheng, B. Huang, X. Qin, X. Zhang, Y. Dai, A controlled anion exchange strategy to synthesize Bi_2S_3 nanocrystals/BiOCl hybrid architectures with efficient visible light photoactivity, Chem Commun (Camb), **48** (2012) 97-99.
26. C. Tang, C. Wang, F. Su, C. Zang, Y. Yang, Z. Zong, Y. Zhang, Controlled synthesis of urchin-like Bi_2S_3 via hydrothermal method, Solid State Sciences, **12** (2010) 1352-1356.
27. H.P. Jiao, X. Yu, Z.Q. Liu, P.Y. Kuang, Y.M. Zhang, One-pot synthesis of heterostructured Bi_2S_3/BiOBr microspheres with highly efficient visible light photocatalytic performance, Rsc Advances, **5** (2015) 16239-16249.
28. W. Wang, H. Cheng, B. Huang, X. Lin, X. Qin, X. Zhang, Y. Dai, Synthesis of $Bi_2O_2CO_3$/Bi_2S_3 hierarchical microspheres with heterojunctions and their enhanced visible light-driven photocatalytic degradation of dye pollutants, Journal of colloid and interface science, **402** (2013) 34-39.
29. S.J.A. Moniz, R. Quesada-Cabrera, C.S. Blackman, J. Tang, P. Southern, P.M. Weaver, C.J. Carmalt, A simple, low-cost CVD route to thin films of $BiFeO_3$ for efficient water photo-oxidation, Journal of Materials Chemistry A, **2** (2014) 2922-2927.